Terr. Atmos. Ocean. Sci., Vol. 31, No. 2, 131-139, April 2020 doi: 10.3319/TAO.2019.11.29.01

The Impacts of cloud condensation nuclei on the extreme precipitation of a monsoon coastal mesoscale convection system

Chun-Yian Su[1], Wei-Ting Chen[1, *], Jen-Ping Chen[1], Wei-Yu Chang[2], and Ben Jong-Dao Jou[1]

[1] *Department of Atmospheric Sciences, National Taiwan University, Taipei City, Taiwan*
[2] *Department of Atmospheric Sciences, National Central University, Taoyuan City, Taiwan*

Article history:
Received 23 April 2019
Revised 18 September 2019
Accepted 29 November 2019

Keywords:
Cloud condensation nuclei, Extreme precipitation, Convection, SoWMEX/TiMREX

Citation:
Su, C.-Y., W.-T. Chen, J.-P. Chen, W.-Y. Chang, and B. J.-D. Jou, 2020: The Impacts of cloud condensation nuclei on the extreme precipitation of a monsoon coastal mesoscale convection system. Terr. Atmos. Ocean. Sci., 31, 131-139, doi: 10.3319/TAO.2019.11.29.01

ABSTRACT

This study investigates the impacts of different types of Cloud Condensation Nuclei (CCN) on the extreme of precipitation and updraft (above the 99th percentile threshold) of a mesoscale convection system occurred over the southwest coast of Taiwan Island under the moist southwesterly monsoon environment using cloud-permitting simulations. The convection system over the Taiwan Strait was observed during the SoWMEX/TiMREX IOP#8 in 2008. Simulations with the maritime type (clean) and the continental type (polluted) CCN are carried out and compared. The polluted simulation exhibits stronger extreme precipitation and updraft. The stronger extreme precipitation is associated with the enhanced size of snow and graupel. The enhanced latent heat release from faster diffusion growth of cloud drops contributes to stronger extreme updraft in the polluted simulation. With smaller rain evaporation rate, cold pool is weaker in the polluted simulation, which also leads to a more optimized convection structure and enhanced extreme updraft. The current results highlight the potential impacts of aerosol loadings on the extreme rainfall of monsoon coastal convection through microphysical, thermodynamics, and dynamical effects.

1. INTRODUCTION

The aerosols-cloud interactions play an important role in the atmospheric radiation budget and hydrological cycle, and the associated processes contribute to the highest uncertainty in the anthropogenic climate forcing (Boucher et al. 2013). By acting as cloud condensation nuclei (CCN), the number of aerosol particles is a key component of the cloud microphysics that can potentially modulate the size of cloud drops (Twomey 1977; Twomey et al. 1984), cloud lifetime (Albrecht 1989; Hansen et al. 1997; Ackerman et al. 2000), and the collision and coalescence processes of raindrop formation (Rosenfeld 1999). For convective clouds, the aerosol-induced microphysical changes become more complex if the mixed-phase processes are involved. The altered microphysical processes and the associated latent heat release may lead to the invigoration of deep convection (Rosenfeld et al. 2008). However, the overall response in clouds and precipitation is also determined by subsequent changes in convective structure, cloud dynamics, and radiative effects, and therefore highly depends on the regimes of the precipitating system being investigated (Stevens and Feingold 2009; Tao et al. 2012; Fan et al. 2013; Tao and Li 2016), the ambient environment condition such as humidity and vertical wind shear (Fan et al. 2012b, 2013; Kalina et al. 2014; Lebo and Morrison 2014; Grant and van den Heever 2015), and the choice of microphysics scheme (Fan et al. 2012a).

The coastal areas over the Asian monsoon region are the occurrence hotspots of mesoscale convection systems with intense extreme rainfall and expansive system size (Hamada et al. 2014). These are also the metropolitan and industrial areas with high urban and/or industrial emissions of aerosols. The impacts of aerosols on the deep convective systems over these areas have been investigated by Fan et al. (2012a, b, 2013) using regional model simulations at cloud-permitting resolutions (~2 km) over southeastern China. Their analyses, which only explored the averaged changes in convection intensity and total precipitation, showed enhancement of these properties under a polluted

* *Corresponding author*
E-mail: weitingc@ntu.edu.tw

aerosol condition, especially under weak wind shear. On the other hand, the modulation of extreme precipitation and updraft by aerosol/CCN loadings over the coastal organized convection in the monsoon environment, which can provide valuable insights to disaster prevention and urban planning, has not yet been systematically studied.

The goal of the current study is to investigate the response of the extreme precipitation and updraft to the different CCN profile in the mesoscale convective system near Taiwan. Here the term "extreme" in this study is defined as instantaneous precipitation (or updraft) intensity above the top 1% (99^{th} percentile) threshold in the frequency distribution. The studied case is a mesoscale convective line embedded in the moist southwesterly monsoon flow observed by the Southwest Monsoon Experiment/Terrain-influenced Monsoon Rainfall Experiment (SoWMEX/TiMREX) in 2008. The intensive radar observations during this case has been applied to understand its mesoscale structure, microphysical characteristics, and precipitation efficiency (Chang et al. 2015; Xu and Zipser 2015), as well as to evaluate and improve a microphysics scheme in the Weather Research and Forecasting (WRF) model (Gao et al. 2011). We carried out two convection-permitting simulations for this case with a horizontal resolution of 1 km at the inner-most domain to resolve the convective processes, each with different CCN scenario using the Chen-Liu-Reisner (CLR) two-moment bulk microphysics scheme (Cheng et al. 2010). Section 2 introduces the synoptic environment and observation for the studied case and the model setup. The simulated results are presented in section 3, while section 4 provides the summary and discussion.

2. METHODOLOGY

2.1 Case Description

The SoWMEX/TiMREX campaign was conducted from 15 May to 26 June in 2008 at the western coastal plain and mountain slope regions of southern Taiwan (Jou et al. 2011). The convection system of interest here occurred on 14 June (IOP#8), embedded in the moist southwesterly monsoon flow after the passage of the Mei-Yu front. The synoptic environment at 0600 UTC from the National Centers for Environmental Prediction (NCEP) final analyses data and the hourly accumulated precipitation from 0300 to 0600 UTC (local time 1100 to 1400) from the Tropical Rainfall Measuring Misson (TRMM) 3B42 are shown in Fig. 1. A Mei-yu front was located in the west side of southern Taiwan stretching from the northern South China Sea through Taiwan Strait to central Taiwan (Wang et al. 2014). A strong southwesterly low-level jet (~25 m s^{-1}) with abundant water vapor appeared between 850 and 700 hPa over the Taiwan Strait, which encountered the mountain slope region of southern Taiwan.

Between 0900 - 1400 UTC on 14 June 2008, a mesoscale convective system in a squall line form propagated southeastward crossing the Taiwan Strait through cold-pool dynamics, mainly due to a strong low-level vertical wind shear environment (Chang et al. 2015; Xu and Zipser 2015). The system was well observed by the National Center for Atmospheric Research S-band dual-polarization (S-POL) radar deployed at the southwest part of Taiwan. Figure 2a shows the observed radar reflectivity at 3 km altitude at 1000 UTC. The signal of radar reflectivity larger than 40 dBZ shows a convective line stretching between 119°E, 22°N and 120.3°E, 23°N, which is the system to be simulated and perturbed by the cloud-permitting model. The northern tip of this system passed the southwestern part of Taiwan around 1200 UTC. During this event, the peak intensity of surface rain rate measured at the Cigu supersite (120.5°E, 22.7°N) reaches 50 mm hr^{-1}.

2.2 Model Configuration and Experimental Setup

The simulations are carried out using the WRF version V3.4.1. There are four two-way nested domains in the simulations (Fig. 1), with spatial resolutions of 27, 9, 3, and 1 km from the outer to the inner domains, respectively. The outer domain covers the whole east Asia (86 - 152°E, 2.5 - 45°N) and the inner domain includes southeastern China, Taiwan Strait, and Taiwan island. The vertical coordinate has 30 layers and the time steps from the outer to the inner domains are 90, 30, 10, and 3.333 seconds, respectively. Kain-Fritsch cumulus parameterization scheme (Kain 2004) is used in the outer domain (27 km), while in the other domains of higher resolution the convective processes are resolved instead of using cumulus parameterization at sub-grid scale. Shortwave and longwave radiation options are Goddard schemes (Chou and Suarez 1999; Chou et al. 2001). The surface layer adopts the MM5 Monin-Obukhov scheme (Beljaars 1995), the boundary layer scheme is the Yonsei University (YSU) scheme (Hong et al. 2006) and the land-surface option is thermal diffusion scheme (Dudhia 1996).

The microphysics scheme used in this study is the Chen-Liu-Reisner (CLR) scheme (Cheng et al. 2010). This is a two-moment bulk microphysics scheme containing the warm cloud processes from the CL scheme (Chen and Liu 2004) and the mixed cloud processes from the Reisner scheme (Reisner et al. 1998). The predicted hydrometeors are mixing ratio of water vapor, mixing ratio and number concentration of cloud water, rain, snow, graupel, and cloud ice. The CCN is assumed to be composed of ammonium sulfate, and its size spectrum is represented by three log-normal distribution (including fine mode, accumulation mode, and coarse mode). The aerosol is initialized as homogeneous in horizontal. Activation of the CCN follows the Kohler theory, with supersaturation resolved with an embedded parcel model. Aerosol restoration from the droplets' evaporation is also calculated in the CLR scheme. The raindrops are generated

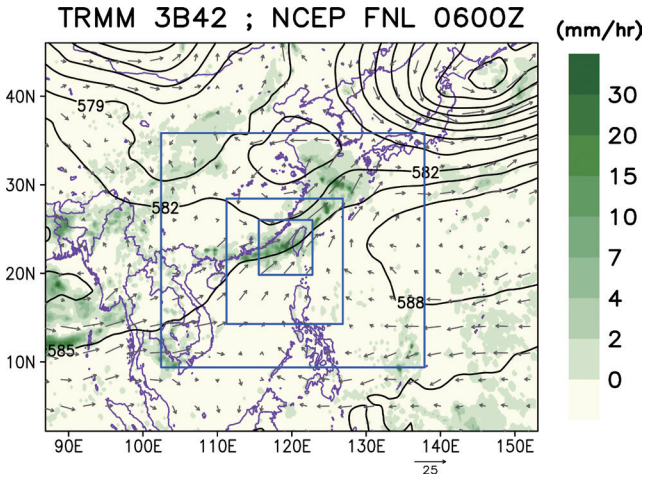

Fig. 1. The synoptic environment during the SoWMEX/TiMREX IOP8 on 14 June 2008: the 500 hPa geopotential height (black lines) and the 700 hPa wind fields (gray arrows) at 0600 UTC from NCEP final operational global analysis data, and the accumulated precipitation (green shading in mm hr^{-1}) between 0300 and 0600 UTC from TRMM 3B42 observations. The blue rectangles show the three inner nested domains used in the WRF simulations.

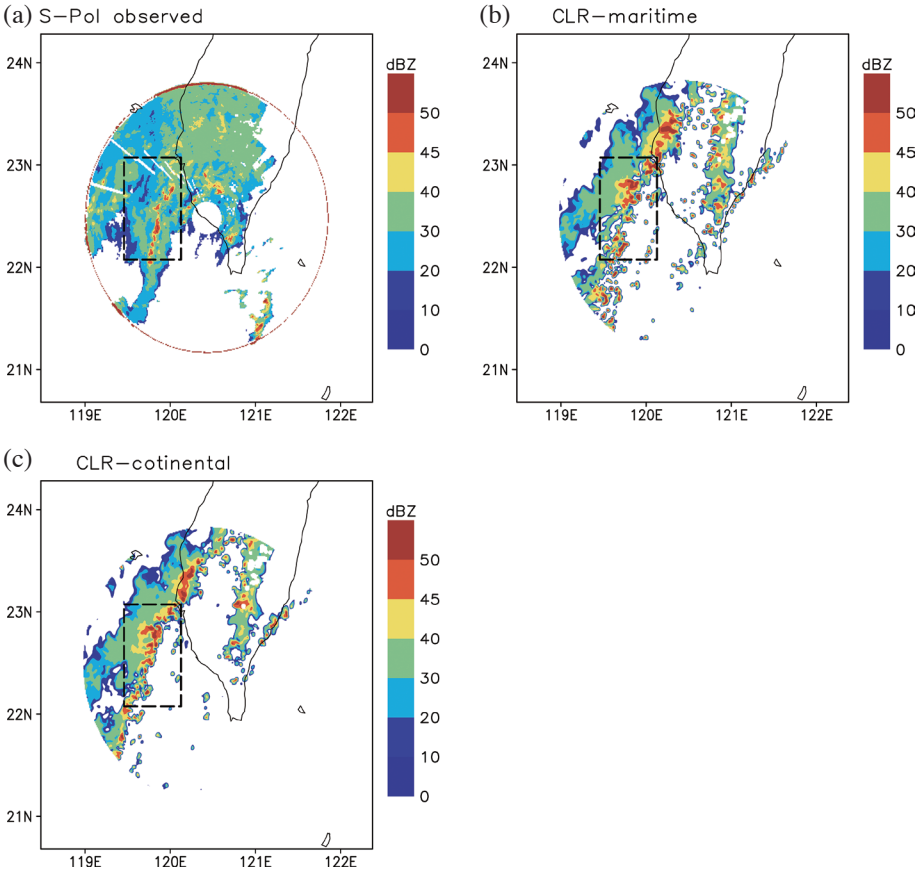

Fig. 2. Radar reflectivity (color shading in dBZ) at 3 km altitude at 1000 UTC on 14 June 2008 from (a) S-Pol radar observations, and the simulations at 1100 UTC with (b) maritime CCN and (c) continental CCN at 2.88 km altitude. The resolution of S-Pol radar observations is 0.01 degree. The red circle represents the detective range of the radar.

by auto-conversion as well as from giant CCN. Two CCN conditions are used in the simulations, namely, the maritime type and the continental type referred to Whitby (1978), to represent the clean and the polluted environment, respectively. The two CCN conditions have different number concentration, modal value of radius, and geometric width of distribution in size spectrum of each mode. The aerosol scale height in the two CCN conditions is also different. As the representative of the discrepancy, the number concentration at standard temperature and pressure for the fine, accumulation, and coarse modes are 340, 60, and 3 cm^{-3} for the maritime type, and 6400, 230, and 3.2 cm^{-3} for the continental type.

The simulations utilize the 1° × 1°, 6-hourly NCEP global analyses data as initial and boundary conditions, starting at 1200 UTC 13 June. The integration is initially carried out using the maritime type CCN, and at 0800 UTC 14 June, the simulation is restarted. One simulation continues to use the maritime type CCN (hereafter CLRM) to represent the clean condition. The other simulation switches to the continental type CCN (hereafter CLRC) after the restart to represent the perturbation by the polluted condition. Both simulations are terminated at 0000 UTC 15 June, and the period to be analyzed and discussed in the next section is between 1030 - 1200 UTC on 14 June 2018, before the system interacts with the complex terrain in Taiwan.

3. RESULT

Figures 2b and c show the simulated radar reflectivity at 3 km altitude in the two simulations at 1100 UTC, the time when the location of the simulated convective line is close to the observation. We note that the simulated system propagates slower compared to the observation. The overall locations of the simulated system in the two simulations with different CCN types are similar. The result suggests that perturbation of the polluted scenario has a small impact on the propagation of the convective system since the synoptic-scale environment is controlled by the initial and boundary condition. The response of the convection features, such as precipitation intensity, hydrometeor vertical profiles, and updraft velocity, to the perturbation of the polluted scenario under similar synoptic-scale environment will be analyzed next over the dashed box in Fig. 2 at 1030 - 1200 UTC.

The probability distribution of precipitation intensity over the convective line is shown in Fig. 3. The precipitation intensity at probability over the top 1 % (99^{th} percentile) ranges from 20 to 90 mm hr^{-1} in the two simulations. Such intensity is close to the definition of "extremely heavy rain" by the Central Weather Bureau in Taiwan (i.e., 24-hr accumulated rainfall exceeds 200 mm or 3-hr accumulated rainfall exceeds 100 mm). The CLRC simulates stronger extreme precipitation intensity compared to the CLRM. The convective line is then separated to convective and stratiform region based on the radar-based partitioning algorithm (Feng et al. 2011). The extreme precipitation in both the convective and stratiform regions is stronger in the CLRC compared to the CLRM, and the strongest precipitation intensity (> 50 mm hr^{-1}) is mostly contributed from the convective region. The production of extreme precipitation is considered to be related to the strength of the updraft. The contoured frequency with altitude diagram (hereafter CFAD) (Yuter and Houze 1995) of vertical velocity is shown in Fig. 4 to show the impacts of different CCN types on the extreme updraft. The CLRC has the stronger updraft at the three probability intervals (top 0.001 - 0.01%, 0.01 - 0.1%, 0.1 - 1%) compared to the CLRM. The strongest updraft in the CLRC (CLRM) is 22 (20) m s^{-1} for probability of top 0.001 - 0.01%, 20 (15) m s^{-1} for probability of top 0.01 - 0.1%, and 10 (8) m s^{-1} for probability of top 0.01 - 0.1%.

Next, the hydrometeors profiles and the dynamical structure of the extreme events are analyzed to understand the potential mechanism that the polluted CCN condition leads to stronger extreme rainfall and updraft in the simulated convective line. Figure 5 shows the vertical profiles of each hydrometeor type conditionally sampled for precipitation intensity stronger than the 99^{th} percentile. Figures 5a and b show the composite mean mass mixing ratio and number concentration, respectively, and Fig. 5c shows the composite mean volume radius ratio (CLRC/CLRM). For cloud water, the mass mixing ratio and the number concentration in the CLRC are higher, and the radius is smaller compared to the CLRM. The result is consistent with the Twomey effect that more cloud droplets can be activated under a more polluted scenario, which leads to smaller size due to the insufficient water vapor. The conversion rate of collision and coalescence from cloud drops into raindrops are mitigated due to smaller cloud drops, and more cloud drops are found ascending above the freezing level.

However, the mixing ratio and the radius of raindrops in the CLRC is still larger compared to the CLRM, which is the source of the stronger extreme precipitation. The larger raindrops could be contributed by the melting of the larger ice-phase particles (i.e., snow and graupel) that are also found in the CLRC. The CLRC has larger snow compared to the CLRM. This is related to the higher number concentration of cloud drops and cloud ice, which leads to the enhancement of the Wegener-Bergeron-Findeisen process. Also, the graupel size in the CLRC is larger, which is associated with the excessive number of cloud drops and cloud ice and conversion from snow. The mixing ratio of graupel is increased while the number concentration of graupel is decreased, owing to the smaller radius of cloud drops and cloud ice which suppresses the conversion of cloud ice to graupel through the riming process. Therefore, although the warm rain processes are suppressed due to the excessive cloud drops, the stronger extreme precipitation can still be found in the CLRC by the melting of the large frozen particles.

The changes in microphysical processes between the two simulations can alter the dynamical structure of the extreme convection through the variation in the latent heating budget. Figure 6 shows a snapshot of the vertical cross-section of perturbation equivalent potential temperature and vertical velocity of the single convective cell in the two simulations, highlighting the relationship between the cold pool and the extreme updraft. In CLRC, which exhibits stronger extreme updraft, the cold pool strength is weaker compared to the CLRM. The lower number concentration of raindrops in CLRC leads to a slower evaporation rate.

In addition, among the microphysical processes, the diffusional growth rate of cloud drops contributes the most to the difference in latent heat budget between the two simulations (figure not shown). Figure 7 demonstrates the difference between the two simulations in latent heating profiles contributed by cloud drop diffusion growth (positive values correspond to higher latent heating in CLRC). The vertical profiles are binned by the vertical velocity at 5.7 km altitude, where the maximum difference in vertical velocity between the two simulations occurs (see Fig. 4). The largest difference in latent heating is found for the vertical velocity stronger than its 99.9th percentile, and the difference becomes small when the vertical velocity is weaker than its 95th percentile. The excessive cloud drops in the CLRC caused stronger latent heat release via diffusion growth than the CLRM, then the intensification of the extreme updraft increases the supersaturation to cloud drops, which leads to the positive feedback further enhancing the latent heat released by diffusion growth of cloud drops. We also note that the latent heating from ice deposition, which is mainly associated with the Wegener-Bergeron-Findeisen process, also contributes to the difference in latent heating, but the magnitude is not as significant as the drop diffusion.

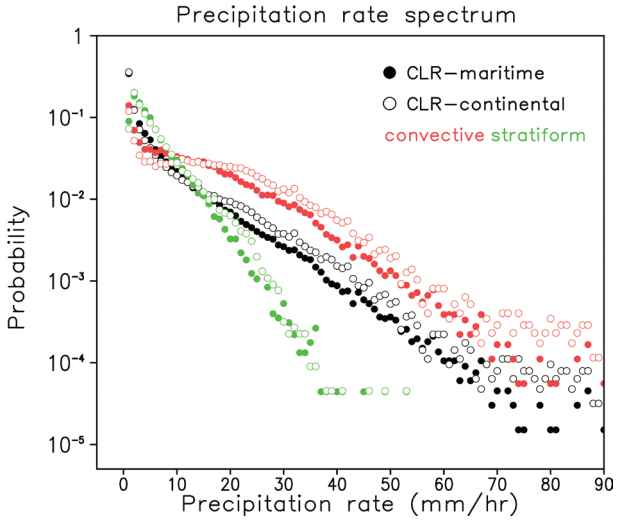

Fig. 3. Probability of precipitation rate intensity with an interval of 1 mm hr^{-1} over the dashed line box in Fig. 2 from 1030 to 1200 UTC simulated using maritime CCN (filled circles) and continental CCN (open circles), probability of precipitation rate intensity over the convective (red) and stratiform (green) regions are also presented.

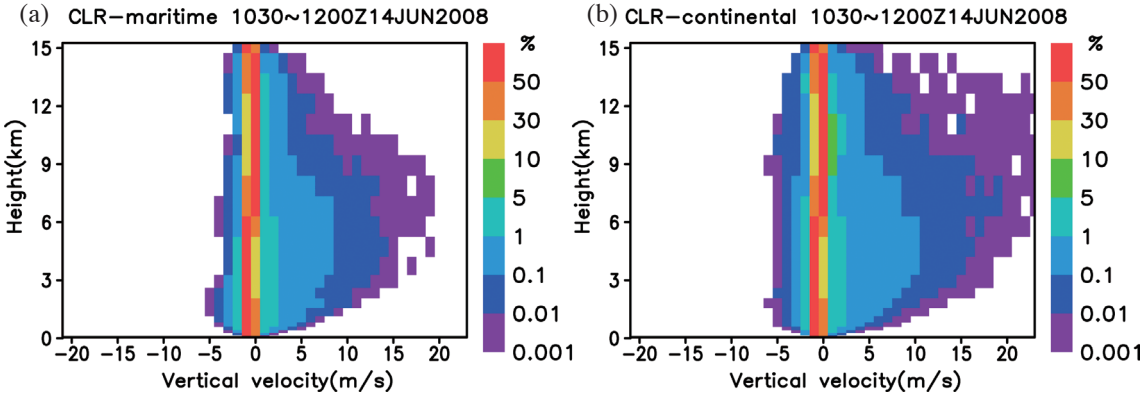

Fig. 4. Vertical velocity CFADs (color shading) over the dashed line box in Fig. 2 on 14 June 2008 constructed from the (a) CLRM and the (b) CLRC from 1030 to 1200 UTC.

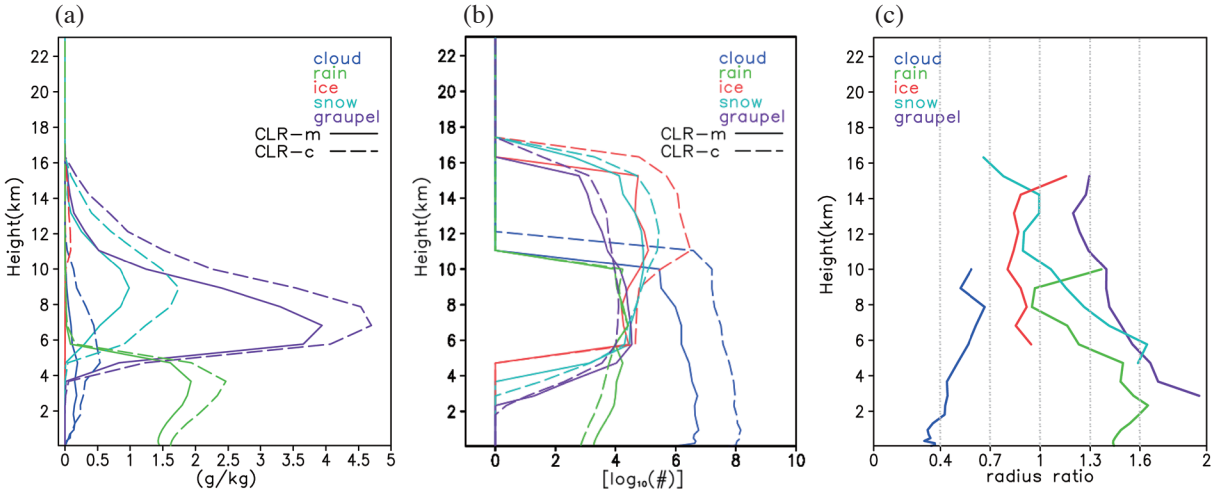

Fig. 5. Vertical profiles of averaged (a) mixing ratios and (b) number concentrations in the CLRM (solid line) and the CLRC (dashed line) and vertical profiles of averaged (c) mean volume radius ratio of the CLRC to the CLRM of various types of hydrometeors where the precipitation rate at the surface is bigger than 99% percentile within the dashed box in Fig. 2 from 1030 to 1200 UTC: rain (green), cloud (blue), ice (red), snow (light blue), and graupel (purple).

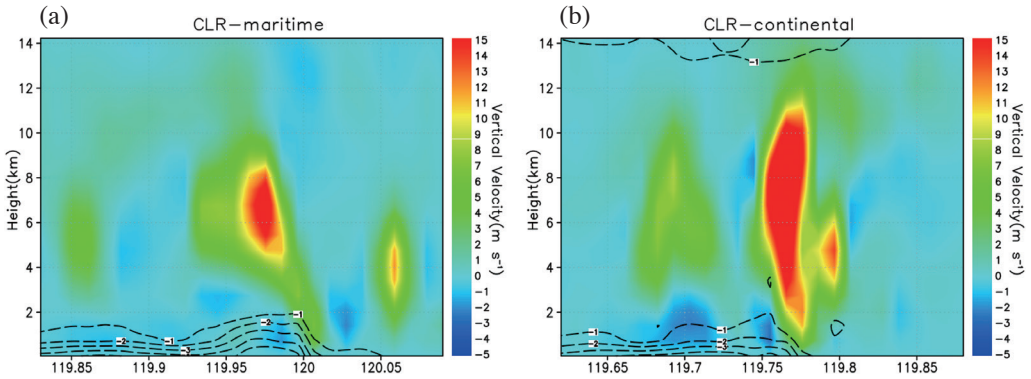

Fig. 6. Snapshots of vertical cross-sections of vertical velocity (color shading) and perturbation equivalent potential temperature (contours) in the CLRM (left) and the CLRC (right).

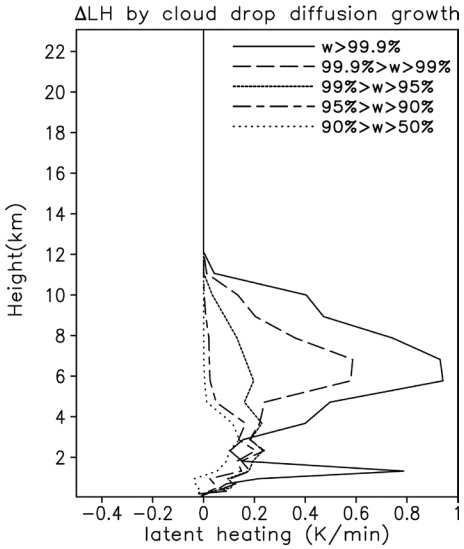

Fig. 7. Difference of the vertical profile of averaged latent heating rate generated by diffusional growth of cloud drops at different percentile interval of vertical velocity at 5.7 km altitude between the CLRC and the CLRM within the dashed box in Fig. 2 from 1030 to 1200 UTC.

4. SUMMARY AND DISCUSSION

This study investigates the impacts of CCN on the extreme (above the 99th percentile threshold) precipitation and updraft in the coastal convective system embedded in the moist southwesterly monsoon flow. The case, which occurred near the southwest coast of Taiwan during the SoWMEX/TiMREX in 2008, is simulated using the WRF model with the CLR two-moment microphysics scheme. Sensitivity to the CCN type is analyzed, focusing on the extreme rainfall and updraft. The results show that the polluted continental CCN condition exhibits stronger extreme precipitation and extreme updraft at the 99th percentile, compared to the cleaner maritime CCN condition. The hydrometeors profiles and the dynamical structure associated with the extreme updraft are summarized in Fig. 8 using the composites of vertical cross-section where vertical velocity at 5.7 km altitude is above the 99.9th percentile. Although the warm rain process is suppressed by the excessive cloud drops in the CLRC, it still has stronger extreme precipitation due to the melting of the large frozen particles.

The cold pool in the CLRC is found to be weaker than the CLRM due to the less raindrop evaporation rate, while the extreme updraft in the CLRC is found being stronger. The result can be explained by the Rotunno-Klemp-Weisman (RKW) theory that the strength of the convection among the convective line is influenced by the relationship between the cold pool strength and the vertical wind shear in the environment. Although the weaker cold pool is found in the CLRC, the favorable combination of vorticity contributed by near-surface temperature gradient and low-level vertical wind shear could be more likely to occur. The tendency of vorticity associated with extreme updraft requires further investigation. Another factor to the stronger extreme updraft in the CLRC is that the diffusion growth rate of cloud drops is faster due to the excessive cloud drops, which contributes to more latent heat compared to the CLRM. The updraft enhanced by the latent heating will increase the supersaturation to cloud drops, which increase the diffusion growth rate of cloud drops again.

We note that the results presented in this study can be sensitive to the microphysics scheme, as revealed in earlier studies (e.g., Fan et al. 2012a). In the future, observations of detailed CCN, hydrometeors, and diabatic profile will be highly useful to evaluate and compare the results of different microphysics scheme. Also, as the response of extreme precipitation to CCN can involve interactions among microphysical, thermodynamic, dynamical, and radiative processes, the piggy-backing method, as proposed by Grabowski (2014), will be applied in the future to delineate the effects between the perturbed microphysics and the subsequent feedbacks.

Acknowledgements We thank the SOWMEX/TIMREX team for providing the radar observation data of the study case. We also thank Dr. Tzu-Chin Tsai for technical assistance on the CLR microphysics scheme. The funding support for this study is from the Ministry of Science and

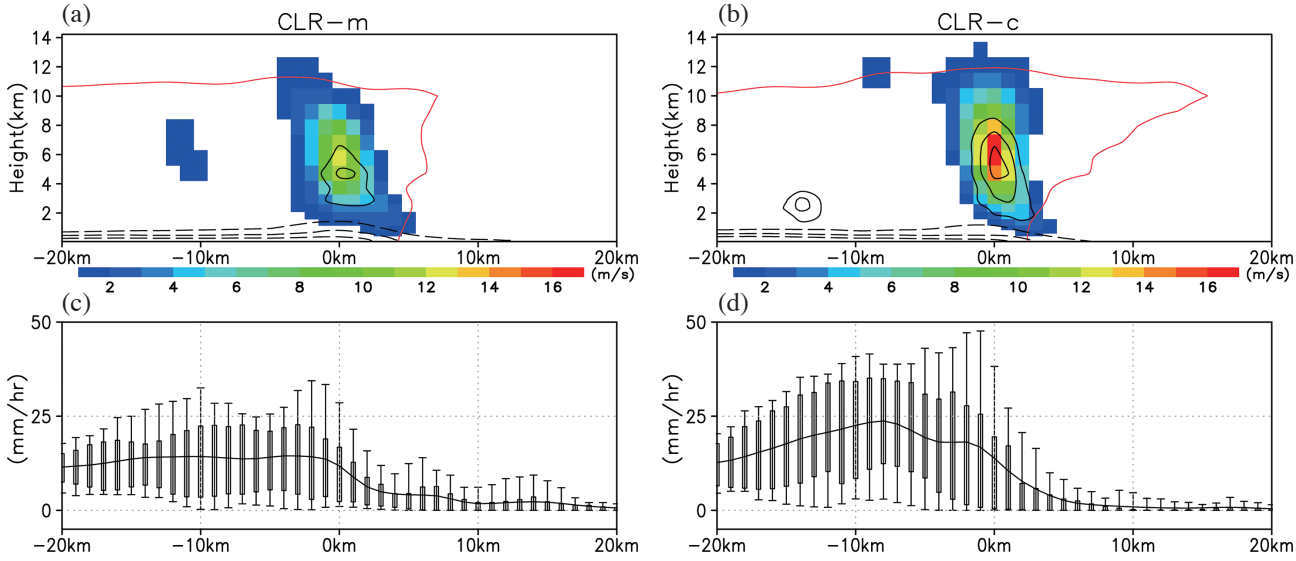

Fig. 8. Composited mean vertical cross-sections of vertical velocity (color shading, negative correspond to downdrafts), latent heating rate caused by cloud drops diffusional growth (contours between 1 and 4 K min^{-1} at an interval of 1 K min^{-1}), radar reflectivity greater than 15 dBZ (red contour), cooling rate caused by raindrop evaporation (purple contours of -0.02, -0.05, -0.1, -0.12 K min^{-1}) and perturbation equivalent potential temperature (black dashed contours between -1 and -3 K at an interval of 1 K). The composite conditionally samples where the vertical velocity at 5.7 km altitude is above 99.9 percentile from 1030 to 1200 UTC on 14 June 2008 simulated in the (a) CLRM and the (b) CLRC. x = 0 corresponds to the location of the strongest updraft at 5.7 km altitude in each simulation. Average precipitation rate in the (c) CLRM and the (d) CLRC. Error bars represent the range between the 10th and 90th percentile, the whiskered boxes represent the range between the first and the third quartile, and lines represent the mean value.

Technology, Taiwan (MOST 106-2111-M-002-005, MOST 107-2119-M-002-024).

REFERENCES

Ackerman, A. S., O. B. Toon, D. E. Stevens, A. J. Heymsfield, V. Ramanathan, and E. J. Welton, 2000: Reduction of tropical cloudiness by soot. *Science*, **288**, 1042-1047, doi: 10.1126/science.288.5468.1042. [Link]

Albrecht, B. A., 1989: Aerosols, cloud microphysics, and fractional cloudiness. *Science*, **245**, 1227-1230, doi: 10.1126/science.245.4923.1227. [Link]

Beljaars, A. C. M., 1995: The parametrization of surface fluxes in large-scale models under free convection. *Q. J. R. Meteorol. Soc.*, **121**, 255-270, doi: 10.1002/qj.49712152203. [Link]

Boucher, O., D. Randall, P. Artaxo, C. Bretherton, G. Feingold, P. Forster, V.-M. Kerminen, Y. Kondo, H. Liao, U. Lohmann, P. Rasch, S. K. Satheesh, S. Sherwood, B. Stevens, and X. Y. Zhang, 2013: Clouds and aerosols. In: Stocker, T. F., D. Qin, G.-K. Plattner, M. Tignor, S. K. Allen, J. Boschung, A. Nauels, Y. Xia, V. Bex, and P. M. Midgley (Eds.), Climate Change 2013: The Physical Science Basis, Contribution of Working Group I to the Fifth Assessment Report of the Intergovernmental Panel on Climate Change, Cambridge University Press, Cambridge, United Kingdom and New York, NY, USA, 571-657.

Chang, W.-Y., W.-C. Lee, and Y.-C. Liou, 2015: The kinematic and microphysical characteristics and associated precipitation efficiency of subtropical convection during SoWMEX/TiMREX. *Mon. Weather Rev.*, **143**, 317-340, doi: 10.1175/mwr-d-14-00081.1. [Link]

Chen, J.-P. and S.-T. Liu, 2004: Physically based two-moment bulkwater parametrization for warm-cloud microphysics. *Q. J. R. Meteorol. Soc.*, **130**, 51-78, doi: 10.1256/qj.03.41. [Link]

Cheng, C.-T., W.-C. Wang, and J.-P. Chen, 2010: Simulation of the effects of increasing cloud condensation nuclei on mixed-phase clouds and precipitation of a front system. *Atmos. Res.*, **96**, 461-476, doi: 10.1016/j.atmosres.2010.02.005. [Link]

Chou, M.-D. and M. J. Suarez, 1999: A solar radiation parameterization for atmospheric studies. Technical Report Series on Global Modeling and Data Assimilation, Volume 15, NASA/TM-1999-104606, NASA Goddard Space Flight Center, Greenbelt, MD United States, 51 pp.

Chou, M.-D., M. J. Suarez, X.-Z. Liang, M. M.-H. Yan, and C. Cote, 2001: A thermal infrared radiation parameterization for atmospheric studies. Technical Report Series on Global Modeling and Data Assimilation, Volume 19, NASA/TM-2001-104606, NASA Goddard Space Flight Center, Greenbelt, MD United States, 68 pp.

Dudhia, J., 1996: A multi-layer soil temperature model for MM5. Proceedings of the 6th PSU/NCAR Mesoscale Model Users' Workshop, Boulder, Colo, USA, 49-50.

Fan, J., L. R. Leung, Z. Li, H. Morrison, H. Chen, Y. Zhou, Y. Qian, and Y. Wang, 2012a: Aerosol impacts on clouds and precipitation in eastern China: Results from bin and bulk microphysics. *J. Geophys. Res.*, **117**, doi: 10.1029/2011jd016537. [Link]

Fan, J., D. Rosenfeld, Y. Ding, L. R. Leung, and Z. Li, 2012b: Potential aerosol indirect effects on atmospheric circulation and radiative forcing through deep convection. *Geophys. Res. Lett.*, **39**, doi: 10.1029/2012gl051851. [Link]

Fan, J., L. R. Leung, D. Rosenfeld, Q. Chen, Z. Li, J. Zhang, and H. Yan, 2013: Microphysical effects determine macrophysical response for aerosol impacts on deep convective clouds. *Proc. Natl. Acad. Sci.*, **110**, E4581-E4590, doi: 10.1073/pnas.1316830110. [Link]

Feng, Z., X. Dong, B. Xi, C. Schumacher, P. Minnis, and M. Khaiyer, 2011: Top-of-atmosphere radiation budget of convective core/stratiform rain and anvil clouds from deep convective systems. *J. Geophys. Res.*, **116**, doi: 10.1029/2011jd016451. [Link]

Gao, W., C.-H. Sui, T.-C. Chen Wang, and W.-Y. Chang, 2011: An evaluation and improvement of microphysical parameterization from a two-moment cloud microphysics scheme and the Southwest Monsoon Experiment (SoWMEX)/Terrain-influenced Monsoon Rainfall Experiment (TiMREX) observations. *J. Geophys. Res.*, **116**, doi: 10.1029/2011jd015718. [Link]

Grabowski, W. W., 2014: Extracting microphysical impacts in large-eddy simulations of shallow convection. *J. Atmos. Sci.*, **71**, 4493-4499, doi: 10.1175/jas-d-14-0231.1. [Link]

Grant, L. D. and S. C. van den Heever, 2015: Cold pool and precipitation responses to aerosol loading: Modulation by dry layers. *J. Atmos. Sci.*, **72**, 1398-1408, doi: 10.1175/jas-d-14-0260.1. [Link]

Hamada, A., Y. Murayama, and Y. N. Takayabu, 2014: Regional characteristics of extreme rainfall extracted from TRMM PR measurements. *J. Clim.*, **27**, 8151-8169, doi: 10.1175/jcli-d-14-00107.1. [Link]

Hansen, J., M. Sato, and R. Ruedy, 1997: Radiative forcing and climate response. *J. Geophys. Res.*, **102**, 6831-6864, doi: 10.1029/96JD03436. [Link]

Hong, S.-Y., Y. Noh, and J. Dudhia, 2006: A new vertical diffusion package with an explicit treatment of entrainment processes. *Mon. Weather Rev.*, **134**, 2318-2341, doi: 10.1175/mwr3199.1. [Link]

Jou, B. J.-D., W.-C. Lee, and R. H. Johnson, 2011: An overview of SoWMEX/TiMREX. In: Chang, C.-P., Y. Ding, N.-C. Lau, R. H. Johnson, B. Wang, and T. Yasunari

(Eds.), The Global Monsoon System: Research and Forecast, 2nd Edition, World Scientific Series on Asia-Pacific Weather and Climate, Volume 5, World Scientific, 303-318, doi: 10.1142/9789814343411_0018. [Link]

Kain, J. S., 2004: The Kain–Fritsch convective parameterization: An update. *J. Appl. Meteorol.*, **43**, 170-181, doi: 10.1175/1520-0450(2004)043<0170:tkcpau>2.0.co;2. [Link]

Kalina, E. A., K. Friedrich, H. Morrison, and G. H. Bryan, 2014: Aerosol effects on idealized supercell thunderstorms in different environments. *J. Atmos. Sci.*, **71**, 4558-4580, doi: 10.1175/jas-d-14-0037.1. [Link]

Lebo, Z. J. and H. Morrison, 2014: Dynamical effects of aerosol perturbations on simulated idealized squall lines. *Mon. Weather Rev.*, **142**, 991-1009, doi: 10.1175/mwr-d-13-00156.1. [Link]

Reisner, J., R. M. Rasmussen, and R. T. Bruintjes, 1998: Explicit forecasting of supercooled liquid water in winter storms using the MM5 mesoscale model. *Q. J. R. Meteorol. Soc.*, **124**, 1071-1107, doi: 10.1002/qj.49712454804. [Link]

Rosenfeld, D., 1999: TRMM observed first direct evidence of smoke from forest fires inhibiting rainfall. *Geophys. Res. Lett.*, **26**, 3105-3108, doi: 10.1029/1999gl006066. [Link]

Rosenfeld, D., U. Lohmann, G. B. Raga, C. D. O'Dowd, M. Kulmala, S. Fuzzi, A. Reissell, and M. O. Andreae, 2008: Flood or drought: How do aerosols affect precipitation? *Science*, **321**, 1309-1313, doi: 10.1126/science.1160606. [Link]

Stevens, B. and G. Feingold, 2009: Untangling aerosol effects on clouds and precipitation in a buffered system. *Nature*, **461**, 607-613, doi: 10.1038/nature08281. [Link]

Tao, W.-K. and X. Li, 2016: The relationship between latent heating, vertical velocity, and precipitation processes: The impact of aerosols on precipitation in organized deep convective systems. *J. Geophys. Res.*, **121**, 6299-6320, doi: 10.1002/2015jd024267. [Link]

Tao, W.-K., J.-P. Chen, Z. Li, C. Wang, and C. Zhang, 2012: Impact of aerosols on convective clouds and precipitation. *Rev. Geophys.*, **50**, doi: 10.1029/2011rg000369. [Link]

Twomey, S., 1977: The influence of pollution on the shortwave albedo of clouds. *J. Atmos. Sci.*, **34**, 1149-1152, doi: 10.1175/1520-0469(1977)034<1149:tiopot>2.0.co;2. [Link]

Twomey, S. A., M. Piepgrass, and T. L. Wolfe, 1984: An assessment of the impact of pollution on global cloud albedo. *Tellus B*, **36**, 356-366, doi: 10.3402/tellusb.v36i5.14916. [Link]

Wang, C.-C., J. Chieh-Sheng Hsu, G. Tai-Jen Chen, and D.-I. Lee, 2014: A study of two propagating heavy-rainfall episodes near Taiwan during SoWMEX/TiMREX IOP-8 in June 2008. Part I: Synoptic evolution, episode propagation, and model control simulation. *Mon. Weather Rev.*, **142**, 2619-2643, doi: 10.1175/mwr-d-13-00331.1. [Link]

Whitby, K. T., 1978: The physical characteristics of sulfur aerosols. In: Husar, R. B., J. P. Lodge, and D. J. Moore (Eds.), Sulfur in the Atmosphere, Pergamon Press, 135-159, doi: 10.1016/B978-0-08-022932-4.50018-5. [Link]

Xu, W. and E. J. Zipser, 2015: Convective intensity, vertical precipitation structures, and microphysics of two contrasting convective regimes during the 2008 TiMREX. *J. Geophys. Res.*, **120**, 4000-4016, doi: 10.1002/2014jd022927. [Link]

Yuter, S. E. and R. A. Houze, 1995: Three-dimensional kinematic and microphysical evolution of Florida cumulonimbus. Part II: Frequency distributions of vertical velocity, reflectivity, and differential reflectivity. *Mon. Weather Rev.*, **123**, 1941-1963, doi: 10.1175/1520-0493(1995)123<1941:tdkame>2.0.co;2. [Link]